RESEARCH ARTICLE

ADVANCED MATERIALS
www.advmat.de

Self-Standing Metal Foam Catalysts for Cathodic Electro-Organic Synthesis

Pavel Moreno-García, María de Jesús de Gálvez-Vázquez, Tobias Prenzel, Johannes Winter, Liliana Gálvez-Vázquez, Peter Broekmann,* and Siegfried R. Waldvogel**

Although electro-organic synthesis is currently receiving renewed interest because of its potential to enable sustainability in chemical processes to value-added products, challenges in process development persist: For reductive transformations performed in protic media, an inherent issue is the limited choice of metallic cathode materials that can effectively suppress the parasitic hydrogen evolution reaction (HER) while maintaining a high activity toward the targeted electro-organic reaction. Current development trends are aimed at avoiding the previously used HER-suppressing elements (Cd, Hg, and Pb) because of their toxicity. Here, this work reports the rational design of highly porous foam-type binary and ternary electrocatalysts with reduced Pb content. Optimized cathodes are tested in electro-organic reductions using an oxime to nitrile transformation as a model reaction relevant for the synthesis of fine chemicals. Their electrocatalytic performance is compared with that of the model CuSn7Pb15 bronze alloy that has recently been endorsed as the best cathode replacement for bare Pb electrodes. All developed metal foam catalysts outperform both bare Pb and the CuSn7Pb15 benchmark in terms of chemical yield and energetic efficiency. Moreover, post-electrolysis analysis of the crude electrolyte mixture and the cathode's surfaces through inductively coupled plasma mass spectrometry (ICP-MS) and scanning electron microscopy (SEM), respectively, reveal the foam catalysts' elevated resistance to cathodic corrosion.

1. Introduction

Electro-organic synthesis provides a highly versatile technique for selective and reagent-free reduction or oxidation of organic compounds under mild reaction conditions.[1] This field is currently undergoing a renaissance because of the urgent need for sustainable chemical processes that can be powered by a surplus of renewable energy.[2] A persistent challenge in cathodic transformations carried out in aqueous media is the limited choice of available materials that are active in the desired transformations and suppress the parasitic hydrogen evolution reaction (HER).[3] Among the materials meeting both requirements, Cd, Hg and particularly Pb have been widely used.[4] However, these materials are often prone to chemical corrosion under cathodic conditions.[5] This corrosion is undesirable not only because of the technological problems posed by low stability of electrolyzer unit components, but also because the synthesis of fine chemicals and pharmaceutically active agents can tolerate only very low amounts of toxic metallic traces that might form during metal dissolution. To avoid the use of pristine Pb, a variety of novel leaded bronze-based cathode materials have been introduced and screened in electro-organic synthesis through empirical investigations.[6] Some of these materials indeed exhibit similar or even enhanced electrocatalytic performance compared to neat Pb, and also are less prone to mechanical and chemical corrosion. Notably, CuSn7Pb15 and related alloys have been deemed a suitable Pb replacement for organic electroreductions and have been successfully applied to a variety of organic electrosyntheses involving diverse substrates.[6b] Motivated by these advancements, we aimed to further improve the catalytic and mechanical performance of leaded metal cathodes through rational design. We prepared these novel cathode materials through the dynamic hydrogen bubble template (DHBT) method.[7] The developed multi-metal foam-type catalysts were subsequently tested as cathodes in the reference electro-organic transformation–arylaldoxime to benzonitrile. Their performance was compared with the one of the reference material CuSn7Pb15. A superior electrocatalytic performance of the foam-type

---

P. Moreno-García, L. Gálvez-Vázquez, P. Broekmann
Department of Chemistry
Biochemistry and Pharmaceutical Sciences
University of Bern
Bern 3012, Switzerland
E-mail: pavel.moreno@unibe.ch; peter.broekmann@unibe.ch

M. de J. de Gálvez-Vázquez, T. Prenzel, J. Winter, S. R. Waldvogel
Department of Chemistry
Johannes Gutenberg-University Mainz
55128 Mainz, Germany
E-mail: waldvogel@uni-mainz.de

S. R. Waldvogel
Institute of Biological and Chemical Systems – Functional Molecular Systems (IBCS-FMS)
Kaiserstraße 12, 76131 Karlsruhe, Germany

The ORCID identification number(s) for the author(s) of this article can be found under https://doi.org/10.1002/adma.202307461

DOI: 10.1002/adma.202307461

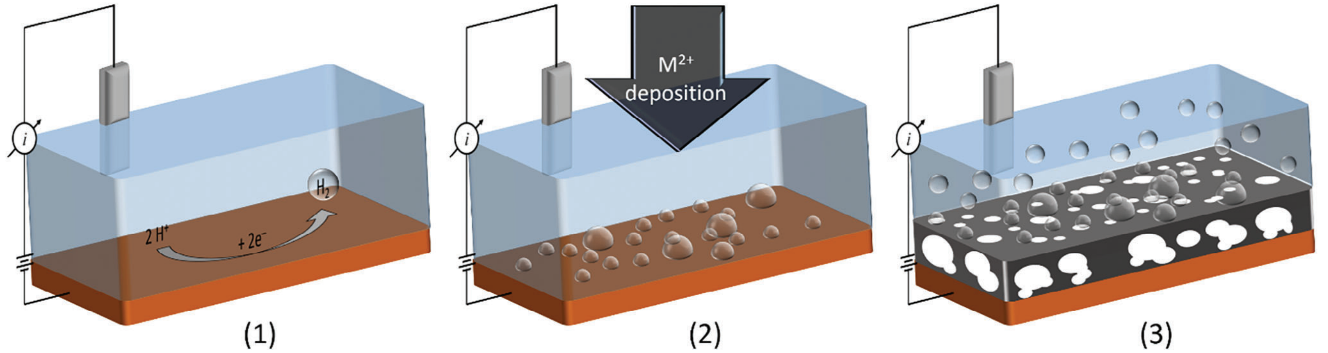

Figure 1. Depiction of the DHBT concept. In the course of electrochemical metal deposition at high current densities in aqueous media, both the HER (1) and metal cation reduction (2) occur simultaneously at the support-electrolyte interface, whereby a highly porous metal foam emerges (3).

materials was validated, and their enhanced mechanical and chemical stability were assessed.

2. Results and Discussion

Self-standing porous metallic materials with unique properties for catalytic applications are of rising interest and are increasingly being prepared through the DHBT approach.[8] **Figure 1** depicts the concept of this manufacturing process, which consists of electrochemical metal deposition from highly acidic aqueous plating baths at current densities ranging from −1 to −10 A cm^{-2}. At such high current densities, the HER (1) occurs concomitantly with the metal cation reduction (2) on the surface of the support to be metallized. Thus, the co-generated hydrogen bubbles impair even growth of the metal layer and serve as a dynamic template for the emerging metal foam.[8b] Typically, after only few seconds have elapsed, hierarchically porous metal foams are achieved (3) that provide intrinsic advantages for electrocatalysis, such as large specific surface areas; high abundance of undercoordinated active sites; and intricate structures that enable reactants or intermediate species to be confined, thereby prolonging their residence times.[8b] These aspects are particularly beneficial in the electrochemical transformations of redox active species that weakly adsorb on electrocatalyst surfaces or require an elevated number of subsequent electron transfer steps.[9]

To develop metal foam electrocatalysts for organic electroreductions with the potential to outperform the planar CuSn7Pb15 reference material, we prepared five DHBT-based series of porous leaded cathodes, which were subsequently screened in electro-organic synthesis experiments. Of note, previous investigations have developed monometallic Pb foams that were tested as cathode materials for electrosynthesis of formate from CO_2.[10] Our leaded foams were prepared on machined Cu slabs under optimized deposition conditions. **Table 1** summarizes the experimental parameters applied to synthesize four binary Cu-*β*-PbO foam series (entries 1–4).[11] The material composition indicated in mass percent was determined by elemental inductively coupled plasma mass spectrometry (ICP-MS) analysis (Table S1, Supporting Information). Further experimental details on sample preparation can be found in the SI file (Figures S1 and S2, Supporting Information). The available catalyst surface area for electro-organic reductions (electrochemically active surface area, ECSA) of the foam-type and the planar CuSn7Pb15 cathodes is also displayed in the rightmost column of Table 1 (additional data in Figure S3, Supporting Information). The developed foams clearly have larger active surface areas than the planar CuSn7Pb15 electrodes.

These materials exhibit two types of porosity: macropores, which are formed by the larger coalesced H_2 bubbles, and micropores, which are created as embedded channels within the walls

Table 1. Experimental parameters used for DHBT-based deposition of leaded alloys. The supporting electrolyte was 0.5 M $HClO_4$ in all cases. [a]The material composition indicated in mass percent was determined by elemental ICP-MS analysis (further information in the SI file). The oxygen content was calculated from the difference between 100% and the measured metal fractions.

Entry	Cathode material[a]	Metal ion source	Deposition t [s]	Applied *j* [A cm^{-2}]	Cathode ECSA [cm^2]
1	Cu21Pb61O18	0.1 M $Cu(ClO_4)_2$ + 0.1 M $Pb(ClO_4)_2$	10	−1	6.90
2	Cu26Pb57O17	0.1 M $Cu(ClO_4)_2$ + 0.1 M $Pb(ClO_4)_2$	20	−1	7.07
3	Cu52Pb30O18	0.15 M $Cu(ClO_4)_2$ + 0.05 M $Pb(ClO_4)_2$	10	−1	5.73
4	Cu49Pb34O17	0.15 M $Cu(ClO_4)_2$ + 0.05 M $Pb(ClO_4)_2$	20	−1	10.25
5	Cu28Sn26Pb37O9	0.1 M $Cu(ClO_4)_2$ + 0.05 M $Pb(ClO_4)_2$ + 0.05 M $SnCl_2$	10	−1	8.14
6	CuSn7Pb15	——	——	——	1.60

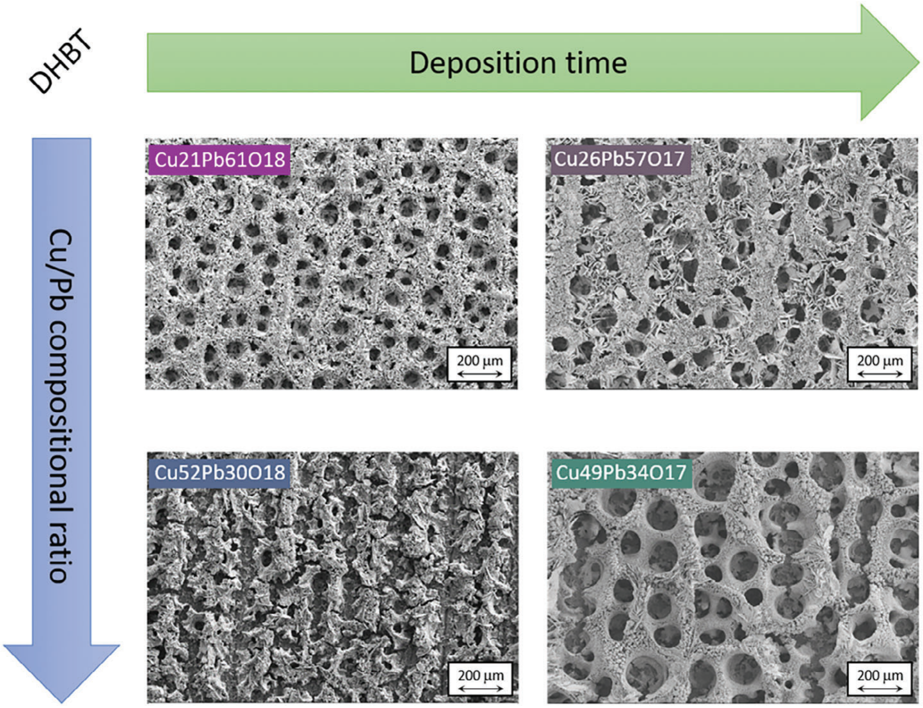

Figure 2. SEM micrographs of as-prepared binary leaded foams (Table 1, entries 1–4). Effects of variations in deposition time and Cu^{2+}/Pb^{2+} concentration ratio on the morphology of Cu-β-PbO binary foams are demonstrated.

of the macropores by smaller H_2 bubbles. **Figure 2** shows representative scanning electron microscopy (SEM) micrographs of these binary foam specimens. The results indicated the effects of varying the applied deposition time and the Cu^{2+}/Pb^{2+} concentration ratio on binary Cu-β-PbO foams (Table 1, entries 1–4). First, the mean surface macropore diameter increased as the deposition time was doubled from 10 to 20 s. This finding occurred because, as the electrolysis proceeds during metal deposition, the size of the macropores tends to increase, thus yielding a hierarchically structured foam deposit that has relatively more small pores close to the support material and fewer but larger pores close to the solution interface.[8b] The pore size distribution, the relative area they occupy on the projected geometric area and the film thickness are shown in Figures S4 and S5 and Tables S2 and S3, Supporting Information, for all leaded foams. Logically, longer deposition times translate into larger foam thicknesses and ECSA values. The thickness of the binary foam materials deposited for 10 s (Cu21Pb61O18 and Cu52Pb30O18) lied in the 70 to 90 μm range. The one of binary systems deposited for 20 s (Cu26Pb57O17 and Cu49Pb34O17) reached up to 120 μm. On the other hand, the ternary foam presented a smaller thickness of ≈40 μm. Second, increasing the ratio of Cu^{2+}/Pb^{2+} precursor from 1 to 3 impaired the continuity of the foam network for the deposits achieved after 10 s. This was less visible for samples that were deposited for 20 s. The occasional discontinuity of the pores might be caused by the increased amount of generated H_2 bubbles on the growing foam walls with higher Cu concentrations (Cu has a significantly larger exchange current density for HER than Pb).[8b]

Energy dispersive X-ray spectroscopy (EDS) elemental mappings corresponding to the samples shown in Figure 2 are displayed in **Figure 3**. The micrographs clearly show that Pb and O are bound to each other and that the surface coverage of this phase increased with lower Cu^{2+}/Pb^{2+} concentration ratios in the plating bath and longer deposition times (Table S4, Supporting Information). The XRD characterization shown in Figure S6, Supporting Information, further confirms that these materials are composed of segregated highly crystalline β-PbO and metallic Cu phases.

Moreover, β-PbO was clearly more abundant than Cu on the surfaces of these metal deposits. This aspect might be advantageous in reductive electrosynthesis, because these materials should, in principle, provide both enhanced corrosion resistance and maintain the intrinsic catalytic properties of Pb. Previous electrosynthesis investigations have demonstrated that cathode materials with adjacent Cu and Pb domains are excellent catalysts for challenging electro-organic reductions, provided that the Cu phase does not favor parasitic side reactions or substrate decomposition.[6b] Moreover, binary systems with adjacent segregated phases can be exploited in sequential systems in which an intermediate formed on one phase further reacts to the target product at the surface of the second component.[12]

Furthermore, to potentially increase the mechanical resistance to corrosion of the electrodeposited leaded foams without substantially compromising the catalytic assets of elemental Pb, we synthesized Pb-containing ternary alloy foams to achieve increased Pb miscibility in the host matrix. To this end, Cu28Sn26Pb37O9 ternary foam cathodes were deposited from the plating bath specified by entry 5 in Table 1. Except for the Sn^{2+} metal ions added to the deposition electrolyte at the expense of the Pb^{2+} ion concentration, all other deposition parameters matched the conditions used to synthesize foam Cu21Pb61O18.

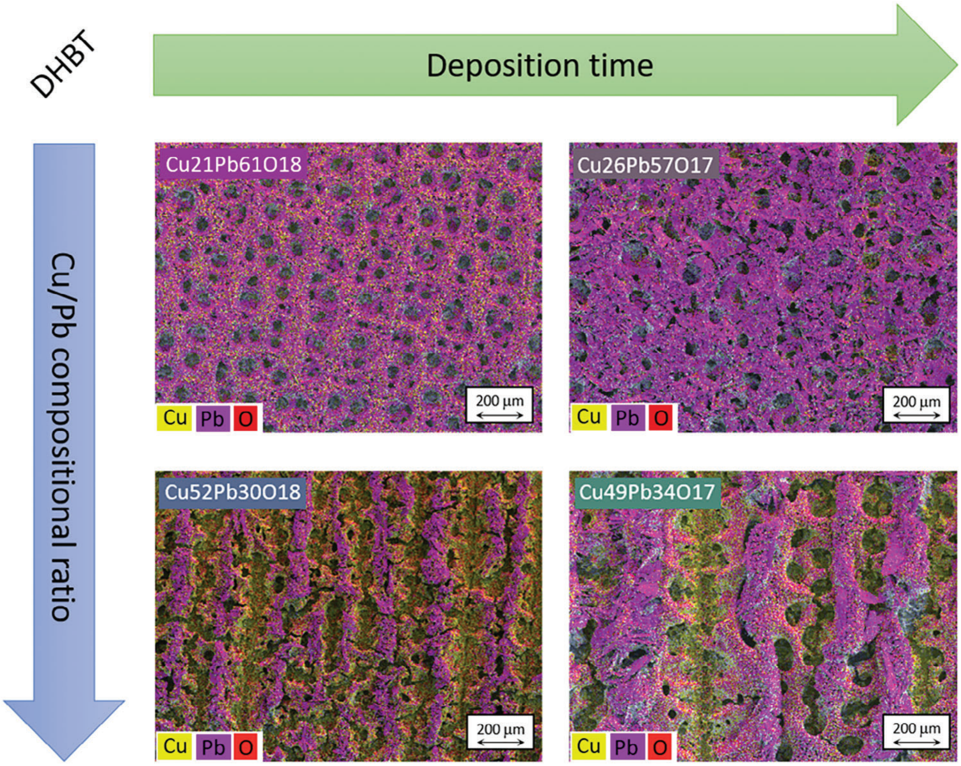

Figure 3. EDS elemental mappings of the as-prepared binary leaded foams. Effects of variations in the deposition time and precursor concentration ratio on the element surface coverage of Cu-β-PbO binary foams are demonstrated.

Figure 4 presents SEM-EDS morphological and compositional comparisons between the binary Cu21Pb61O18 and the three-component Cu28Sn26Pb37O9 leaded bronze foams. The left upper panels of Figure 4 show representative SEM micrographs of a binary Cu21Pb61O18 specimen at different magnifications. This material exhibits a fairly inhomogeneous morphology and is composed of hexagonally faceted micrometer-sized platelet-like features adjacent to smaller, round cauliflower-like clusters. The corresponding EDS elemental mapping on the right demonstrates the high segregation of platelets and

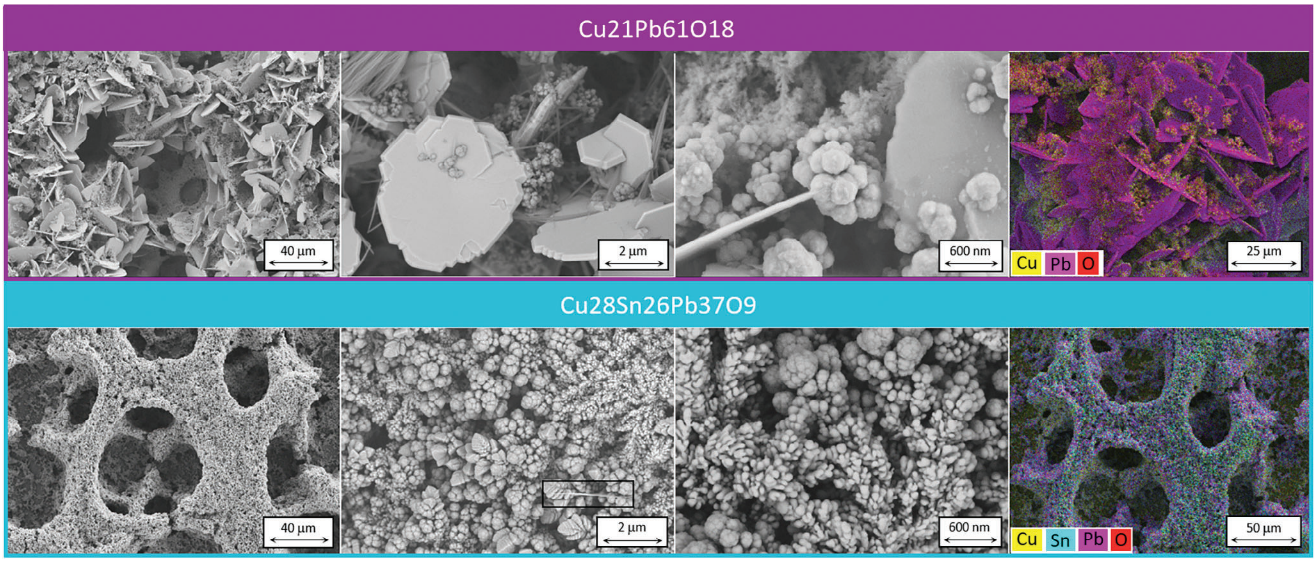

Figure 4. Top view SEM-EDS micrographs of the as-prepared leaded foams Cu21Pb61O18 and Cu28Sn26Pb37O9. Morphological and compositional segregation are clear from the SEM and EDS analyses, respectively, of the Cu-β-PbO binary foams. In contrast, the ternary foam specimens show a more homogeneous micro-structured skeleton and element distribution.

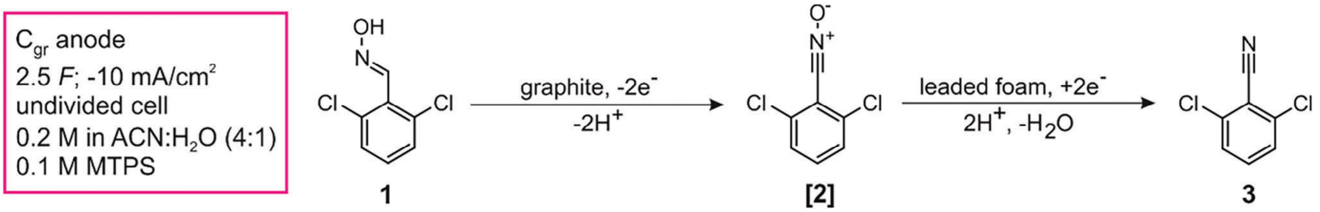

Scheme 1. Reaction pathway and applied experimental conditions for the electrochemical reduction of 2,6-dichlorobenzaldoxime (**1**) to 2,6-dichlorobenzonitrile (**3**), tested on leaded foam alloys. This reaction is within the framework of domino oxidation-reduction sequences, in which the intermediate [**2**] is obtained after oxidation of (**1**) on the graphite anode before its reduction to the nitrile derivative (**3**) on the surfaces of the leaded foams. C_{gr}, ACN and MTPS indicate graphite, acetonitrile and methyltripropylammonium methylsulfate, respectively.

cauliflower-type clusters consisting of β-PbO and Cu, respectively. The observed phase segregation was not unexpected, given that Pb is well known to be only marginally soluble when alloyed in a Cu matrix (<0.09 at% at 600 °C).[13] This elemental immiscibility of the binary foams might initially seem disadvantageous, because bare Pb typically undergoes mechanical and chemical degradation during the course of reductive electrolysis.[6b] The lower panels in Figure 4 instead show that the framework of Cu28Sn26Pb37O9 is composed of fairly porous walls with sub-micrometer-sized particulate building blocks that are compactly linked and are scarcely disrupted by highly faceted, impermeable and segregated micrometer-sized β-PbO platelets (black frame in the second panel from the left). The corresponding XRD characterization in Figure S6, Supporting Information, demonstrates that bare Pb and β-PbO are absent in the bulk of this ternary foams. EDS analysis indicated that the proportion of segregated Pb and β-PbO on the surface of Cu28Sn26Pb37O9-type foams was significantly lower than observed on the surfaces of all other foam cathode materials. This finding was due primarily to the elevated miscibility of Pb in both pristine Sn and CuSn alloy domains. Of note, in several surface regions, Cu remained slightly segregated (Figures S6 and S7, Supporting Information). Thus, the ternary foams apparently have four advantageous characteristics: i) enhanced mechanical robustness of their skeletons; ii) better resistance to Pb corrosion; iii) relatively higher amounts of undercoordinated active sites; and iv) longer, narrower, unobstructed channels, in which reactants and intermediates can be retained for longer times, thus facilitating their transformation before they leave the porous structure. The latter two points seem to be supported by the larger ECSA value of Cu28Sn26Pb37O9 compared to the ones of binary systems with the same deposition time (Cu21Pb61O18 and Cu52Pb30O18).

To validate the suitability of the prepared leaded foam cathode materials for reductive electro-organic synthesis, we selected the transformation of oximes to nitriles as a test vehicle. Specifically, the electroreduction of 2,6-dichlorobenzaldoxime **1** to 2,6-dichlorobenzonitrile **3** (**Scheme 1** and S1) was screened on all Cu-supported leaded foams. Noteworthy, the scope of this generic transformation can be extended to a range of interesting substrates (Scheme S2, Supporting Information).[14]

The electrolyte and electrolysis conditions (e.g., solvent, supporting electrolyte, current density, applied charge and anode material) proposed and optimized by Gütz et al.[6b] to achieve the best product selectivity and yields on flat CuSn7Pb15 leaded bronze alloys were applied, as displayed at the left of Scheme 1. Detailed descriptions of the electrolysis experiments and product yield quantification are provided in the SI file (Figures S8–S12, Supporting Information). Notably, all electrolyzes were performed at an optimized geometric current density of −10 mA cm^{-2}.[6b] Consequently, the amount of applied charge through the solid liquid interface was distributed along larger sample surfaces in foam-type catalysts than in planar cathode materials, such as the reference CuSn7Pb15 (Table 1 and Figure S3, Supporting Information). Therefore, the leaded foams were subjected to milder stress conditions during electrosynthesis, thus potentially enhancing their resistance to chemical and mechanical degradation and therefore, prolonging their operational use. Noteworthy, long-term stability of electrodes is a critical aspect in the later translation into technical application.[15]

Table 2. Obtained yields and cell voltages of the domino-oxidation-reduction sequence 2,6-dichlorobenzaldoxime **1** to 2,6-dichlorobenzonitrile **3** on different cathode materials in an undivided cell.

Entry	Cathode material	Yield [%]	Cell voltage [V]
1	Cu21Pb61O18	81	−2.97
2	Cu26Pb57O17	78	−3.02
3	Cu52Pb30O18	75	−2.93
4	Cu49Pb34O17	78	−3.03
5	Cu28Sn26Pb37O9	80	−2.88
6	Pb	67	−3.44
7	CuSn7Pb15	75	−3.05

Table 2 summarizes the reaction yields of the 2,6-dichlorobenzaldoxime to 2,6-dichlorobenzonitrile electroreduction on all tested cathode materials. In agreement with earlier reports, the flat reference materials Pb and CuSn7Pb15 provided good product yields of 67% and 75%, respectively (entries 6 and 7).[6b] To our knowledge, these are the highest reported yields for this specific halogen-free direct electro-organic transformation on Pb-derived materials. Beyond exhibiting better catalytic performance than pristine Pb, CuSn7Pb15 is a mechanically more robust material for electro-organic synthesis.[6b] Entries 1–5 in Table 2 display the product yields obtained on the developed leaded foams. All binary and ternary foam alloys outperformed bare Pb. Moreover, with the exception of foam Cu52Pb30O18, they also outperformed the reference CuSn7Pb15. The highest achieved yields were obtained with the binary Cu21Pb61O18 (81%) and the ternary Cu28Sn26Pb37O9

(80%) systems (identified side products in low yields are shown in Scheme S3 and Figures S13 and S14, Supporting Information). Yields obtained at non-optimal higher current densities were significantly lower (e.g., 49% on Cu21Pb61O18 at 25 mA cm^{-2}). The improved performance of the developed leaded foams was also confirmed by comparative cyclic voltammetry of the intermediate nitrile oxide [**2**] using selected leaded and bare metal cathodes. The catalytic capabilities of the investigated materials shown in Figure S15, Supporting Information, follow the trend Cu21Pb61O18 > Cu28Sn26Pb37O9 > Pb ≈ CuSn7Pb15 ≈ Sn. This demonstrates that the enhanced yields originate not only from the larger ECSA values of the foams but also from their intrinsic catalytic nature. We suggest that the increased catalytic effect of leaded foam-type materials might originate from their elevated porosity and highly crystalline and edgy morphologies that provide comparably many more undercoordinated active sites than flat polycrystalline materials (ECSA values in Table 1 and Figures 2–5 and Figures S3–S6, Supporting Information).

Furthermore, since the electrosyntheses are performed in an ACN:H_2O (4:1) mixture, elucidation of the parasitic HER on the best performing foam Cu21Pb61O18 and the flat CuSn7Pb15 benchmark was conducted. To this end, dedicated electrosyntheses were coupled to online H_2 detection by gas chromatography. Figure S16, Supporting Information shows that after a short time, electrogeneration of H_2 is completely suppressed on the surface of both leaded materials. The short-lived HER contribution is due to the lack of intermediate **[2]** on the surface of the cathodes at the beginning of the electrosyntheses (Scheme S1). As soon as [**2**] reaches the cathode surfaces after its electrogeneration on the anode, the targeted electroreduction is significantly favored and the concentration of generated H_2 drops down to negligible values.

Importantly, not only the product selectivity on the developed cathode materials but also the process efficiency was enhanced, since the cell voltage developed during the course of the galvanostatic electrolysis was lower when the foam-based cathodes were used (fourth column in Table 2). This aspect is frequently overlooked, yet greatly affects the viability and sustainability of an electricity-fed synthetic approach at industrial scale.[9] Finally, to demonstrate the reusability of the foam cathodes we conducted longer performance tests consisting of four consecutive electrolysis cycles using a single Cu21Pb61O18 specimen. The reaction yields remained rather constant after each subsequent iteration and the cathode underwent no major dissolution (Table S5, Supporting Information).

We suggest that these results are already promising on their own from an electrocatalytic standpoint. Nevertheless, for electrosynthesis of fine chemicals and pharmaceutical active agents, the prevention of cathode corrosion during electrolysis (particularly in the case of Pb, Cd or Hg) is just as important as its catalytic properties. We therefore performed post-electrosynthesis experiments allowing chemical and mechanical degradation assessment of the cathode materials induced by the applied electrosynthesis. This should provide an additional measure to assess the suitability of the foam cathodes for reductive organic electrosynthesis.

Regardless of the cathode material used (e.g., Pb, CuSn7Pb15 or leaded metal foams), all solutions became slightly yellowish as the electrosynthesis proceeded (comparison of Figures S8 and S17, Supporting Information). This color might have originated not only from the buildup of the reaction products but also from cathode dissolution. The latter would clearly undermine the suitability of the developed foams as cathode materials for organic electrosynthesis in realistic applications. To identify possible cathode dissolution, we conducted quantitative elemental ICP-MS analysis of the crude electrolyzed mixture for selected samples. The experimental details of this post-electrosynthesis metal quantification in the reaction medium are provided in the SI file.

Table 3 summarizes the concentrations of dissolved metals found in the crude at the end of the electrolyzes performed with the flat CuSn7Pb15 sample, the binary Cu21Pb61O18 and the ternary Cu28Sn26Pb37O9 foam-type materials. In all cases, not only the corrosion prone Pb but also Cu underwent dissolution. However, both foam cathodes were more resistant to Pb corrosion than the planar CuSn7Pb15 reference material. These results suggested that the DHBT method induced enhanced mechanical stability of electrochemically deposited Pb in combination with Cu and CuSn alloy. Unexpectedly, the binary Cu21Pb61O18 foam was the most robust material. Note also that the ECSA of the foam-type electrodes was significantly larger than that of the planar CuSn7Pb15 reference material (Table 1); consequently, the amount of dissolved metal per unit surface area of cathode material was substantially lower for the foam-type electrodes (normalized metal concentrations in columns 5–7 of Table 3). Additionally, the same qualitative trend was observed for Pb content after work-up. Finally, after product isolation by column chromatography the Pb content decreased significantly.

Furthermore, we performed complementary degradation investigations of the cathode materials to provide direct insight into their mechanical endurance in the performed electrolyzes. Identical location SEM (IL-SEM) studies involved inspecting and comparing identical sample regions before and after organic electrosynthesis screening.[16] This analytical technique provides insight through detailed information on the morphological transformations that non-colloidal electrocatalysts undergo as a result of electrolysis experiments.[17] These investigations were performed on dedicated CuSn7Pb15, Cu21Pb61O18 and Cu28Sn26Pb37O9 specimens that were subjected to identical galvanostatic electrosyntheses, as described above. Representative results are displayed in **Figure 5** and Figure S18, Supporting Information. The findings clearly indicated that the surface of CuSn7Pb15 underwent substantial morphological alterations originating from the applied electrochemical process (Figure 5a). Features that were easily recognizable before and after electrosynthesis are framed in green. Some of these features arose from the machining step applied to prepare the CuSn7Pb15 specimens. The bright features on the surfaces of the CuSn7Pb15 cathodes before the electroreduction have previously been identified as segregated Pb domains by multiple analytical techniques (laser ablation mass spectrometry, scanning Auger microscopy, energy-dispersive X-ray spectroscopy and X-ray fluorescence spectroscopy).[6b,c,18] The lower panels in Figure 5a demonstrate that these Pb aggregates were so prone to cathodic corrosion that they disappeared almost quantitatively from the cathode surface after the applied electrolysis (sample regions encircled in red). This observation correlated with the large amount

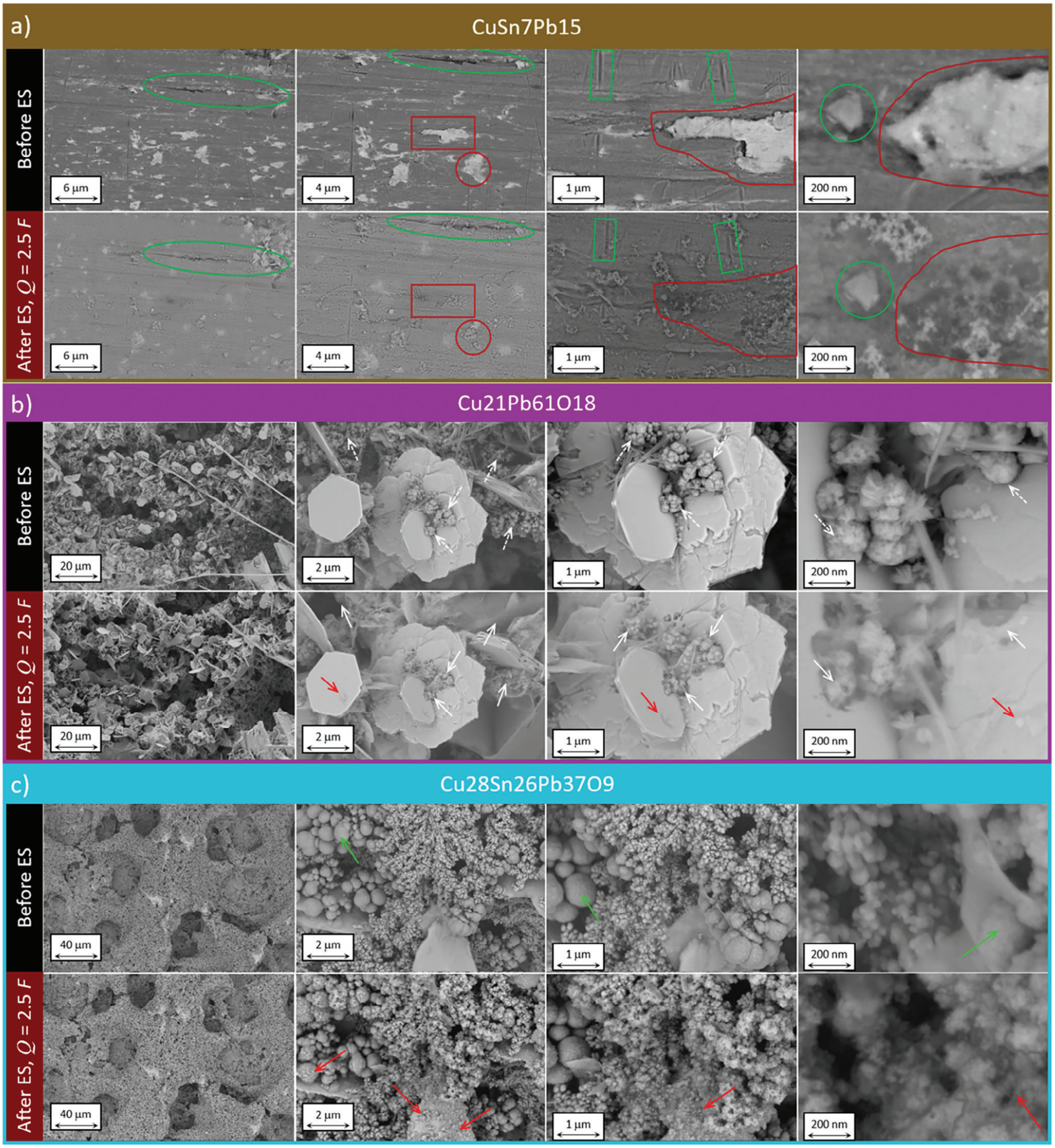

Figure 5. IL-SEM investigations on different catalyst types before and after electroreductions ($j = -10$ mA cm^{-2}, $Q = 2.5$ F and $\omega = 400$ rpm). a) CuSn7Pb15. Surface features that are recognizable both before and after the electrolysis are enclosed by green shapes, whereas surface features that disappeared after electrolysis are framed in red. In contrast, b) Cu21Pb61O18 and c) Cu28Sn26Pb37O9 undergo substantially milder mechanical degradation. The white arrows point to sample locations where the material underwent dissolution after electrosynthesis (ES). The red arrows point to redeposited material. The green arrows indicate spherical CuSn particles that underwent no apparent degradation.

Table 3. ICP-MS elemental analysis of the crude after electrosynthesis. Amounts of dissolved Cu, Sn and Pb in the crude after electrosynthesis on the surfaces of selected cathode materials. Metal concentrations after work-up and product isolation are also shown. NA indicates non-available and corresponds to concentrations below the used calibration range.

Cathode material	Dissolved Cu in the crude [ppm]	Dissolved Sn in the crude [ppm]	Dissolved Pb in the crude [ppm]	Normalized [Cu] [g cm^{-2}]	Normalized [Sn] [g cm^{-2}]	Normalized [Pb] [g cm^{-2}]	[Cu] after work-up [ppm]	[Sn] after work-up [ppm]	[Pb] after work-up [ppm]	[Cu] after isolation [ppm]	[Sn] after isolation [ppm]	[Pb] after isolation [ppm]
Cu21Pb61O18	9.25	NA	14.84	9.38×10^{-6}	NA	1.51×10^{-5}	0.28	NA	0.16	NA	NA	2.6×10^{-3}
Cu28Sn26Pb37O9	24.44	20.34	16.24	2.1×10^{-5}	1.75×10^{-5}	1.40×10^{-5}	3.02	0.09	0.33	NA	8.9×10^{-3}	6.0×10^{-2}
CuSn7Pb15	11.37	1.30	34.01	4.97×10^{-5}	5.69×10^{-6}	1.49×10^{-4}	1.59	0.18	0.65	NA	3.0×10^{-2}	6.1×10^{-2}

of dissolved Pb revealed by ICP-MS analysis of the crude when CuSn7Pb15 was used as cathode material. In contrast, SEM analysis of the binary foam Cu21Pb61O18 revealed only minor morphological alterations caused by the electrolysis (Figure 5b). This finding is remarkable since the outermost surface of β-PbO is possibly reduced to metallic Pb under the reductive conditions enforced during cathodic electrosynthesis. Nevertheless, the abundant highly crystalline hexagonal β-PbO platelets did not undergo structural rearrangements. This correlated with the lowest concentration of dissolved Pb in the crude for the electrolysis performed on this binary system (Table 3). In contrast, the adjacent nanometer-sized cauliflower-like Cu particles did lose a fraction of their mass, which either diffused into the crude or was redeposited at other sample locations. The dotted white arrows in the upper panels point to such nanoparticulate Cu structures, which were somewhat dissolved and were only partly present after the electrolysis in the lower panels (solid white arrows). Of note, partial redeposition of dissolved Cu was observed on the surfaces of the flat β-PbO platelets (red arrows in the lower panels). Figure 5c displays the IL-SEM analysis of the ternary leaded foam. The scarce crystalline β-PbO flakes underwent no visible degradation, similarly to the binary foam case. The green arrows in the central panels point to round CuSn particles that were barely altered by the electrolysis (Figure 5c and Figure S7, Supporting Information). However, the smaller PbSn cauliflower-like particles (Figure S7, Supporting Information) did undergo mild agglomeration. The red arrows in the lower panels point to redeposited material on the surface of both the CuSn particles and the flat β-PbO flakes. Unexpectedly, this finding suggested that Pb stability was impaired when alloyed with Sn with respect to that in the β-PbO phase. Considering the results shown in Table 3, we suggest that these minor morphological changes in Cu28Sn26Pb37O9 did not significantly contribute to the accumulation of catalyst material (mainly Pb) in the crude during the course of the electrosynthesis.

Complementary EDS elemental mappings were obtained on the same sample locations displayed in Figure 5 (**Figure 6**, additional data in Figure S19 and Table S6, Supporting Information). Figure 6a shows the data corresponding to CuSn7Pb15. The pre-electrosynthesis mappings revealed segregated Pb-rich clusters embedded in the surface of the CuSn matrix. As deduced from the IL-SEM investigations, the post-electrolysis EDS micrographs unambiguously confirmed the nearly complete depletion of unalloyed Pb from the cathode surface. These elemental mappings together with the morphological characterizations in Figure 5a allowed us to exclude substantial redeposition of dissolved Pb on the surface of the catalyst material. Thus, the eroded Pb ultimately polluted the reaction medium. Interestingly, Figures 5b and 6b show that both the sharp edges and smooth surfaces of the hexagonal β-PbO flakes did not wear away. Instead, the sub-micrometer Cu particles were somewhat eroded. The dotted white arrows in the upper panels of Figure 6b point to Cu agglomerates that underwent partial corrosion and became less voluminous after the organic electroreduction was completed (solid white arrows in the lower panels). Although some of the dissolved Cu was found in the crude, a fraction was clearly redeposited at adjacent regions of the catalyst surface (indicated by red arrows). Notably, despite being composed primarily of immiscible micrometer-sized β-PbO grains, these electrochemically

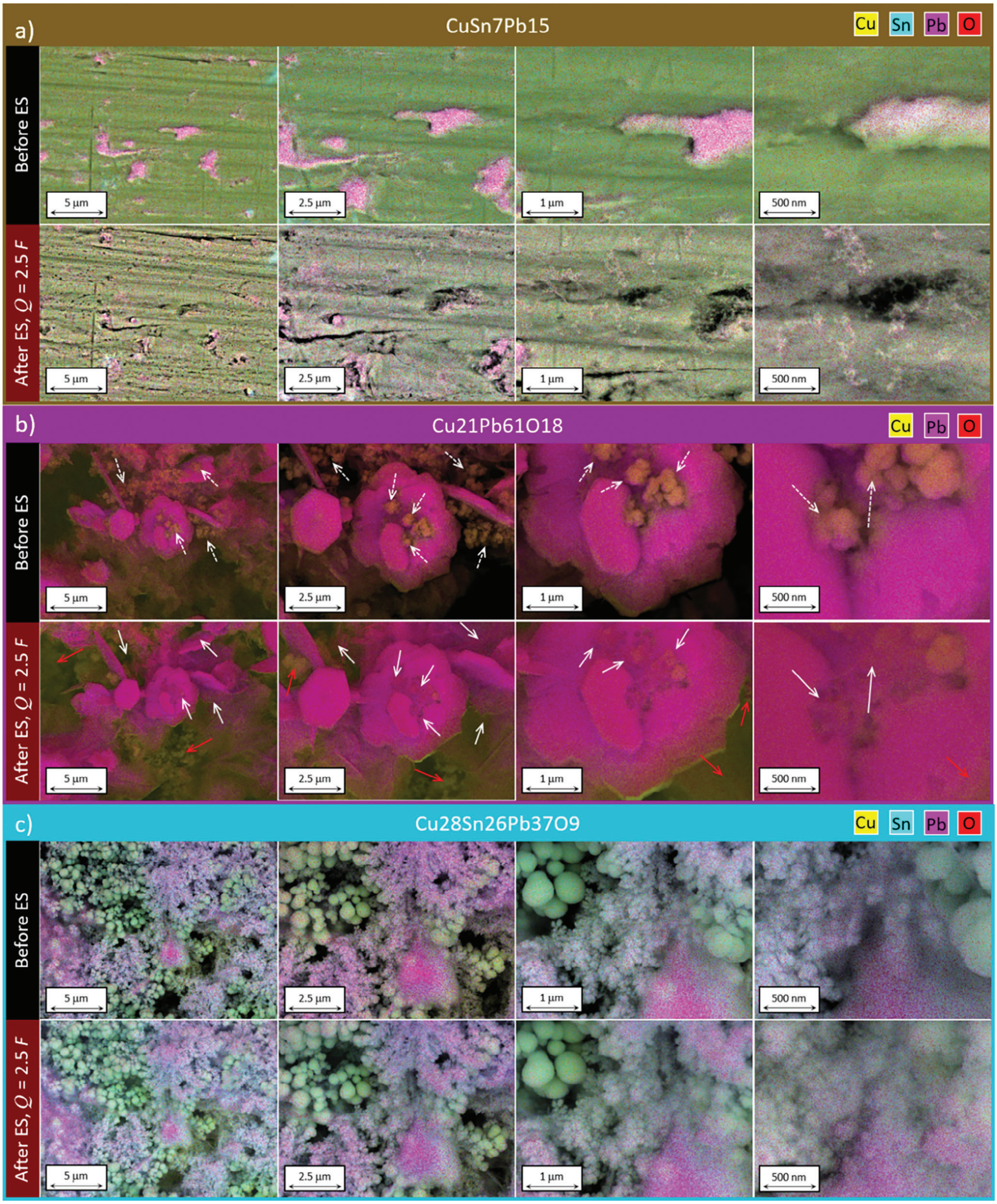

Figure 6. IL-EDS investigations of different catalyst types before and after electroreductions (j = −10 mA cm^{-2}, Q = 2.5 F and ω = 400 rpm). a) CuSn7Pb15. Pb-rich domains embedded in the bronze matrix undergo massive dissolution. Comparably, the harder host CuSn matrix remains almost intact. b) The hexagonally faceted β-PbO platelets on the surface of Cu21Pb61O18 are mechanically robust. Only the smaller, less abundant cauliflower-like Cu particles experienced partial dissolution. c) The elemental surface distribution of Cu28Sn26Pb37O9 undergoes only minor alterations as a result of electro-organic synthesis. ES indicates electrosynthesis.

deposited Cu-β-PbO binary foams were remarkably less prone to corrosion than both neat Pb and planar leaded bronze alloys. On the one hand, this finding might have been due to the lower effective current densities enforced on the foam-type materials than on flat cathodes during electroreduction. On the other hand, the increases in chemical and structural stability might have also originated from the highly crystalline surface finish of the β-PbO platelets achieved with the DHBT method (Figure S6, Supporting Information).[17b,19] Hagihara et al. have suggested that atoms embedded in planes with higher in-plane packing are relatively more resistant to chemical corrosion because of their higher atomic coordination and stronger atomic bonding.[20] Indeed, the hexagonal faceting of the β-PbO platelets provides such high in-plane packing on their surfaces. Finally, in agreement with the SEM-based analysis of Cu28Sn26Pb37O9, the corresponding IL-EDS analysis (Figure 6c) indicated barely noticeable compositional alterations on the surface of this material. As mentioned above, the scarce β-PbO flakes and the round CuSn-rich particles were particularly robust and did not exhibit any observable erosion. Comparison of the SEM and EDS analysis at the highest applied magnifications suggested that only the smaller cauliflower-type PbSn nanoparticles were altered by agglomeration and dissolution (Figure S6b). Together, the ICP-MS and IL-SEM-EDS results suggested that a fraction of the dissolved material diffused into the electrolyte, whereas the remaining portion was redeposited along the foam surface.

Overall, the degree of chemical and mechanical degradation undergone by the electrodeposited leaded foams was clearly milder than that of the CuSn7Pb15 reference material, which has recently been endorsed as suitable replacement for Pb in organic electroreductions performed in aqueous media. In addition, the superior electrocatalytic performance of these foams was demonstrated through a relevant oxime to nitrile electro-organic reduction, which can be extended to a range of interesting substrates.

3. Conclusion

To avoid the use of highly toxic Pb cathode materials in electroorganic synthesis, we developed novel leaded metal foam-type electrodes through the DHBT method. These materials feature large specific surface areas, high abundance of undercoordinated active sites and intricate structures that enable the beneficial confinement of reactants or intermediate species for prolonged residence times. In a demonstrative example, these materials were tested in electro-organic reductions using an oxime to nitrile transformation relevant to the synthesis of fine chemicals (synthesis of 2,6-dichlorobenzonitrile from 2,6-dichlorobenzaldoxime). Their electrocatalytic performance was contrasted with that of the model CuSn7Pb15 leaded alloys that have recently been deemed the best cathode replacement for bare Pb electrodes. All developed metal foam catalysts outperformed both bare Pb and CuSn7Pb15 in terms of chemical yields. In addition, post electrolysis analyses of the crude electrolyzed mixture and the cathode's surfaces through ICP-MS and SEM, respectively, were conducted to assess their possible degradation. The leaded metal foams were found to be mechanically more robust and substantially less prone to cathodic corrosion than both planar cathodes Pb and CuSn7Pb15. Consequently, they were demonstrated to be better suited for electro-reductive organic transformations relevant for fine chemicals and pharmaceutically active agents, in which only very low traces of toxic metallic contaminations are tolerated that might form by cathode dissolution.

Supporting Information

Supporting Information is available from the Wiley Online Library or from the author.

Acknowledgements

P.M.-G. and M.d.J.G.-V. contributed equally to this work. This publication was created as part of NCCR Catalysis (grant number 180544), a National Centre of Competence in Research funded by the Swiss National Science Foundation. M.d.J.G.-V. acknowledges the Postdoc. Mobility fellowship program (grant number P500PN_210727) of the Swiss National Science Foundation (SNSF). Support by Deutsche Forschungsgemeinschaft (DFG – WA1276/31-1) and Forschungsinitiative Rheinlandpfalz within the frame of SusInnoScience is highly appreciated.

Open access funding enabled and organized by Projekt DEAL.

Conflict of Interest

The authors declare no conflict of interest.

Data Availability Statement

The data that support the findings of this study are available in the supplementary material of this article. The raw data to this paper is made accessible to the public via Zenodo (https://doi.org/10.5281/zenodo.10008022).

Keywords

cathodic corrosion, dynamic hydrogen bubble template, electro-organic synthesis, identical location SEM, metal electrodeposition, metal foam catalyst

Received: July 26, 2023
Revised: October 19, 2023
Published online:

---

[1] a) B. A. Frontana-Uribe, R. D. Little, J. G. Ibanez, A. Palma, R. Vasquez-Medrano, *Green Chem.* **2010**, *12*, 2099; b) D. Pollok, S. R. Waldvogel, *Chem. Sci.* **2020**, *11*, 12386; c) J. L. Röckl, D. Pollok, R. Franke, S. R. Waldvogel, *Acc. Chem. Res.* **2020**, *53*, 45; d) J. L. Röckl, D. Schollmeyer, R. Franke, S. R. Waldvogel, *Angew. Chem., Int. Ed.* **2020**, *59*, 315; e) J. L. Röckl, D. Schollmeyer, R. Franke, S. R. Waldvogel, *Angew. Chem.* **2020**, *132*, 323.

[2] a) M. Yan, Y. Kawamata, P. S. Baran, *Chem. Rev.* **2017**, *117*, 13230; b) M. D. Kärkäs, *Chem. Soc. Rev.* **2018**, *47*, 5786; c) A. Wiebe, T. Gieshoff, S. Möhle, E. Rodrigo, M. Zirbes, S. R. Waldvogel, *Angew. Chem., Int. Ed.* **2018**, *57*, 5594; d) A. Wiebe, T. Gieshoff, S. Möhle, E. Rodrigo, M. Zirbes, S. R. Waldvogel, S. R. Waldvogel, *Angew. Chem.* **2018**, *130*, 5694; e) S. R. Waldvogel, B. Janza, *Angew. Chem., Int. Ed.* **2014**, *53*, 7122; f) S. R. Waldvogel, B. Janza, *Angew. Chem.* **2014**, *126*, 7248.

[3] a) M. C. Leech, K. Lam, *Nat. Rev. Chem.* **2022**, *6*, 275; b) A. Shatskiy, H. Lundberg, M. D. Kärkäs, *ChemElectroChem* **2019**, *6*, 4067; c) S.

Möhle, M. Zirbes, E. Rodrigo, T. Gieshoff, A. Wiebe, S. R. Waldvogel, *Angew. Chem., Int. Ed.* **2018**, *57*, 6018; d) S. Möhle, M. Zirbes, E. Rodrigo, T. Gieshoff, A. Wiebe, S. R. Waldvogel, *Angew. Chem.* **2018**, *130*, 6124.

[4] a) M. I. Montenegro, D. Pletcher, E. A. Liolios, D. J. Mazur, C. Zawodzinski, *J. Appl. Electrochem.* **1990**, *20*, 54; b) J. Kulisch, M. Nieger, F. Stecker, A. Fischer, S. R. Waldvogel, *Angew. Chem., Int. Ed.* **2011**, *50*, 5564; c) J. Kulisch, M. Nieger, F. Stecker, A. Fischer, S. R. Waldvogel, *Angew. Chem.* **2011**, *123*, 5678.

[5] a) R. D. Armstrong, K. L. Bladen, *J. Appl. Electrochem.* **1977**, *7*, 345; b) K. H. Roll, *Ind. Eng. Chem.* **1953**, *45*, 2210; c) S. Stohs, *Free Radical Biol. Med.* **1995**, *18*, 321; d) J. Jörissen, B. Speiser, in *Organic Electrochemistry*, (Ed.: O. S. Hammerich, B.), CRC Press Taylor & Francis Group, Boca Raton **2016**. e) T. Wirtanen, T. Prenzel, J.-P. Tessonnier, S. R. Waldvogel, *Chem. Rev.* **2021**, *121*, 10241.

[6] a) J. Strehl, C. Kahrs, T. Müller, G. Hilt, J. Christoffers, *Chemistry* **2020**, *26*, 3222; b) C. Gütz, V. Grimaudo, M. Holtkamp, M. Hartmer, J. Werra, L. Frensemeier, A. Kehl, U. Karst, P. Broekmann, S. R. Waldvogel, *ChemElectroChem* **2018**, *5*, 247; c) M. D. J. Gálvez-Vázquez, P. Moreno-García, H. Guo, Y. Hou, A. Dutta, S. R. Waldvogel, P. Broekmann, *ChemElectroChem* **2019**, *6*, 2324; d) T. Wirtanen, E. Rodrigo, S. R. Waldvogel, *Chemistry* **2020**, *26*, 5592; e) C. Gütz, M. Selt, M. Bänziger, C. Bucher, C. Römelt, N. Hecken, F. Gallou, T. R. Galvão, S. R. Waldvogel, *Chemistry* **2015**, *21*, 13878.

[7] a) C. A. Marozzi, A. C. Chialvo, *Electrochim. Acta* **2000**, *45*, 2111; b) N. D. Nikolic, K. I. Popov, L. J. Pavlovic, M. G. Pavlovic, *J. Electroanal. Chem.* **2006**, *588*, 88.

[8] a) H.-C. Shin, M. Liu, *Chem. Mater.* **2004**, *16*, 5460; b) S. Vesztergom, A. Dutta, M. Rahaman, K. Kiran, I. Zelocualtecatl Montiel, P. Broekmann, *ChemCatChem* **2021**, *13*, 1039; c) M. Wang, X. Yu, Z. Wang, X. Gong, Z. Guo, L. Dai, *J. Mater. Chem. A* **2017**, *5*, 9488; d) B. J. Plowman, L. A. Jones, S. K. Bhargava, *Chem. Commun.* **2015**, *51*, 4331; e) H.-C. Shin, J. Dong, M. Liu, *Adv. Mater.* **2003**, *15*, 1610.

[9] a) D. M. Heard, A. J. J. Lennox, *Angew. Chem., Int. Ed.* **2020**, *59*, 18866; b) D. M. Heard, A. J. J. Lennox, *Angew. Chem.* **2020**, *132*, 19026.

[10] a) S. Cherevko, X. Xing, C.-H. Chung, *Appl. Surf. Sci.* **2011**, *257*, 8054; b) M. Fan, S. Garbarino, G. A. Botton, A. C. Tavares, D. Guay, *J. Mater. Chem. A* **2017**, *5*, 20747; c) J. Wang, H. Wang, Z. Han, J. Han, *Front. Chem. Sci. Eng.* **2015**, *9*, 57.

[11] a) S. Sawatani, S. Ogawa, T. Yoshida, H. Minoura, *Adv. Funct. Mater.* **2005**, *15*, 297; b) C. G. Poll, D. J. Payne, *Electrochim. Acta* **2015**, *156*, 283; c) L. Meng, J. Ustarroz, M. E. Newton, J. V. Macpherson, *J. Phys. Chem. C* **2017**, *121*, 6835.

[12] A. Dutta, I. Z. Montiel, R. Erni, K. Kiran, M. Rahaman, J. Drnec, P. Broekmann, *Nano Energy* **2020**, *68*, 104331.

[13] D. J. Chakrabarti, D. E. Laughlin, *Bull. Alloy Phase Diagrams* **1984**, *5*, 503.

[14] a) M. F. Hartmer, S. R. Waldvogel, *Chem. Commun.* **2015**, *51*, 16346; b) T. Wirtanen, E. Rodrigo, S. R. Waldvogel, *Adv. Synth. Catal.* **2020**, *362*, 2088.

[15] a) J. Seidler, J. Strugatchi, T. Gärtner, S. R. Waldvogel, *MRS Energy & Sustainability* **2021**, *7*, 42; b) C. Gütz, B. Klöckner, S. R. Waldvogel, *Org. Process Res. Dev.* **2016**, *20*, 26; c) M. Hielscher, E. K. Oehl, B. Gleede, J. Buchholz, S. R. Waldvogel, *ChemElectroChem* **2021**, *8*, 3904; d) M. Dörr, M. M. Hielscher, J. Proppe, S. R. Waldvogel, *ChemElectroChem* **2021**, *8*, 2621.

[16] N. Hodnik, M. Zorko, M. Bele, S. Hocevar, M. Gaberscek, *J. Phys. Chem. C* **2012**, *116*, 21326.

[17] a) M. D. J. Gálvez-Vázquez, P. Moreno-García, H. Xu, Y. Hou, H. Hu, I. Z. Montiel, A. V. Rudnev, S. Alinejad, V. Grozovski, B. J. Wiley, M. Arenz, P. Broekmann, *ACS Catal.* **2020**, *10*, 13096; b) P. Moreno-García, N. Schlegel, A. Zanetti, A. Cedeño López, M. D. J. Gálvez-Vázquez, A. Dutta, M. Rahaman, P. Broekmann, *ACS Appl. Mater. Interfaces* **2018**, *10*, 31355.

[18] V. Grimaudo, P. Moreno-García, A. Riedo, S. Meyer, M. Tulej, M. B. Neuland, M. Mohos, C. Gütz, S. R. Waldvogel, P. Wurz, P. Broekmann, *Anal. Chem.* **2017**, *89*, 1632.

[19] a) N. Nikolic, P. Zivkovic, S. Stevanovic, G. Brankovic, *J. Serb. Chem. Soc.* **2016**, *81*, 553; b) A. Rebey, R. Hamdi, B. Hammami, *Eur. Phys. J. Plus* **2022**, *137*, 295.

[20] K. Hagihara, M. Okubo, M. Yamasaki, T. Nakano, *Corros. Sci.* **2016**, *109*, 68.